Acta Mechanica Sinica (2020) 36(4):775–788
https://doi.org/10.1007/s10409-020-00970-3

RESEARCH PAPER

Numerical implementation and evaluation of resolvent-based estimation for space–time energy spectra in turbulent channel flows

Bowen Yang[1,2] · Guodong Jin[1,2] · Ting Wu[1] · Zixuan Yang[1,2] · Guowei He[1,2]

Received: 15 March 2020 / Revised: 19 May 2020 / Accepted: 4 June 2020 / Published online: 25 July 2020
© The Chinese Society of Theoretical and Applied Mechanics and Springer-Verlag GmbH Germany, part of Springer Nature 2020

Abstract
Resolvent operator has been increasingly used to investigate turbulent flows and develop control strategies. Recently, Towne et al. (J Fluid Mech 883:A17, 2020) proposed a resolvent-based estimation (RBE) method for predicting turbulent statistics in a channel flow. In this paper, we utilize the RBE method to predict the root-mean-square (RMS) and space–time energy spectra of streamwise velocity fluctuation, where the input is the space–time energy spectra at a reference horizontal plane located in the logarithmic layer and the output is the space–time energy spectra in the buffer layer. The explicit formulas for the RBE method are given in detail for numerical implementation. The results show the capability of the RBE method in the prediction of the convection velocity and bandwidth of the space–time energy spectra. Furthermore, we make a systematic evaluation of the performance of the RBE method by varying the input configurations, including the wall-normal location of the reference plane, the inclusion or exclusion of the pressure as an input variable, the implementation approach of the pressure boundary condition, and the choice of the window function. It is found that the results of both RMS velocity and space–time energy spectra obtained from the RBE method are sensitive to the location of the reference plane. However, the pressure boundary conditions and inclusion of pressure as an input do not cause significant change in the RMS velocity and space–time energy spectra. Although it does not influence the prediction of the RMS velocity, a window function is found crucial in the RBE method for the prediction of the space–time energy spectra.

Keywords Space–time energy spectra · Turbulent channel flow · Resolvent operator

1 Introduction

Space–time energy spectra are used to describe turbulent flows in a wavenumber–frequency space to provide a precise assessment of the characteristic length and time scales of turbulent motions. Therefore, the space–time energy spectra are fundamental for the investigations of dynamical coupling among turbulent motions at different scales [1] with broad applications in the noise [2], wind energy [3], and wave–turbulence interactions [4]. In order to obtain the complete space–time energy spectra, the dataset of the flow field in the problem of interest needs to cover all the length and time scales, ranging from the Kolmogorov scales to the integral scales. This requirement is challenging for both numerical simulations and experimental measurements. Specifically, to contain the largest scale of turbulent motions, the spatial domain needs to be sufficiently large, while the time duration needs to be sufficiently long. Meanwhile, to capture the turbulent fluctuations at the smallest scales, the spatial resolution needs to be fine, while the sampling frequency needs to be high. As a result, the computational cost is prohibitively high to obtain the data at all scales [5], especially for turbulent flows at high Reynolds numbers, while the experimental measurements of time-resolved three-dimensional flow fields are also expensive [6,7]. Furthermore, storage resources needed for saving the simulation or measurement data are enormous. These challenges are even more critical in wall-bounded turbulence, due to the presence of large-scale coherent structures [8–10]. To overcome the difficulties in the data acquirement and the limitation in the storage resources, various statis-

✉ Zixuan Yang
yangzx@imech.ac.cn

[1] State Key Laboratory of Nonlinear Mechanics, Institute of Mechanics, Chinese Academy of Sciences, Beijing 100190, China

[2] School of Engineering Sciences, University of Chinese Academy of Sciences, Beijing 100049, China

tical reconstruction methods and theoretical models for the prediction of the space–time energy spectra have been developed.

Statistical reconstruction methods [11–13] are developed to predict the space–time energy spectra using the time series of measurement data at two neighboring points, which provide the frequency spectra at these two points. In these models, a transfer function is applied to reconstruct the energy distribution over different wavenumbers at each given frequency to obtain the space–time energy spectra. Due to the restriction of measurement resolution, it is challenging to provide accurate measurement data for the statistical reconstruction methods in the buffer layer. Based on the random sweeping hypothesis [14,15], theoretical models not relying on the measurement data are derived to predict the space–time energy spectra [16,17], which show agreement with the large-eddy simulation (LES) results in the logarithmic layer of turbulent channel flows. Similar to the statistical reconstruction methods, the theoretical models focus on the space–time energy spectra in the logarithmic layer. Considering the dominant contribution of the buffer layer to the energy production in wall-bounded turbulence [18] and noting that turbulent statistics in the logarithmic region are relatively easy to obtain, it is useful to develop a predictive model to estimate space–time energy spectra in the buffer layer using available data in the logarithmic layer.

Marusic et al. [19,20] develops a predictive model for streamwise velocity fluctuation in the buffer layer of a wall-bounded turbulent flow by accounting for the superposition and modulation effects of very large scale motions in the logarithmic region. This model first obtains a "universal signal" in the buffer layer through simultaneous measurements at two points (one in the buffer layer and the other in the logarithmic region). The universal signal can be regarded as the near-wall velocity fluctuations without the influence of any very large scale motions, which is found insensitive to the Reynolds numbers. The universal signal and the measured large-scale motion in the logarithmic region are then used to reconstruct the time series of the streamwise velocity fluctuation in the buffer layer, of which the statistics are in agreement with those obtained directly from the measurements. Following the pioneering work of Marusic et al. [19,20], other predictive models are proposed based on a similar philosophy [21–23]. However, the outputs of these models are either time series of velocity fluctuations at a single spatial point [21,22] or a flow field in a wall-parallel plane at a specific time instant [23], while the complete space–time energy spectra are unavailable.

Following the previous works for estimating flow statistics from a limited set of known value [24–26], Towne et al. [27] further proposes the resolvent-based estimation (RBE) method for mapping the space–time energy spectra in the logarithmic layer to the space energy spectra in the buffer layer. This method is developed based on the resolvent analysis of McKeon and Sharma [28], in which the transport equations of velocity fluctuations are linearized to formulate an input–output linear dynamical system. The nonlinear terms are treated as an excitation of the linear system, while the velocity fluctuations are the outputs. The Reynolds stresses terms are approximated using an eddy-viscosity model [29–35]. The RBE method makes a good prediction of the profiles of root-mean-square (RMS) of velocity fluctuations below the reference plane. In particular, the location and magnitude of the peak of the streamwise RMS velocity are predicted accurately.

The objective of the present paper is to use the RBE method to predict the space–time energy spectra in the buffer layer of a turbulent channel flow. We also conduct a systematic examination of predictive performance of the RBE method under different parametric configurations, including the location of the reference plane, the implementation approach of the pressure boundary condition, and inclusion or exclusion of pressure fluctuations as an input, and the choice of the window function. In Sect. 2, we present the numerical implementation of the RBE method. The formulas for the RBE method presented in this section can be found in [27]. In Sect. 3, the numerical set-up and data processing procedure are described. In Sect. 4, the RBE method is used to predict the space–time energy spectra in the buffer layer from those in the logarithmic region. Conclusions are drawn in Sect. 5.

2 Implementation of the RBE method

Towne et al. [27] proposed the RBE method to predict the energy spectra in the buffer layer using the known spectra at a reference plane in the logarithmic layer of a turbulent channel flow. We introduce the concept of resolvent operator in turbulent channel flows in Sect. 2.1 and present the numerical implementation of the RBE method in Sect. 2.2.

2.1 Resolvent operator for turbulent channel flows

Figure 1 shows the sketch of the turbulent channel flow under investigation. The coordinates in the streamwise, wall-normal, and spanwise directions are denoted as x, y, and z, respectively, and the components of velocity fluctuations in the corresponding directions are denoted as u, v, and w, respectively. The RBE method is developed based on the resolvent formula [28], of which the derivation starts from the following non-dimensionalized continuity and momentum equations of velocity fluctuations

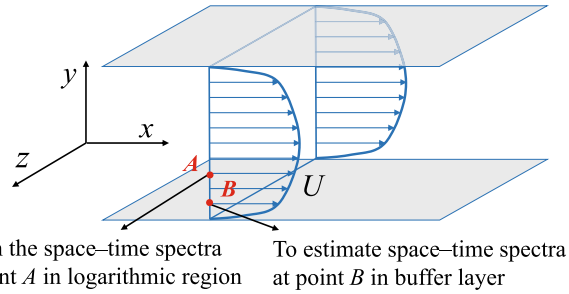

Fig. 1 Schematic illustration of spectra-estimation problem in turbulent channel flow

$$\nabla \cdot \boldsymbol{u} = 0, \tag{1}$$

$$\frac{\partial \boldsymbol{u}}{\partial t} + (\boldsymbol{u} \cdot \nabla)\,\boldsymbol{U} + (\boldsymbol{U} \cdot \nabla)\,\boldsymbol{u} + \nabla p - \frac{1}{Re_\tau}\nabla^2 \boldsymbol{u} = -(\boldsymbol{u} \cdot \nabla)\,\boldsymbol{u} + \langle (\boldsymbol{u} \cdot \nabla)\,\boldsymbol{u} \rangle, \tag{2}$$

where $\boldsymbol{U} = [\boldsymbol{U}(y), 0, 0]^{\mathrm{T}}$ is the mean velocity, $\nabla = [\partial/\partial x, \partial/\partial y, \partial/\partial z]^{\mathrm{T}}$ is the gradient operator, p is the pressure fluctuation, $\langle \cdot \rangle$ represents an ensemble averaging. All the variables are non-dimensionalized using one-half the channel height h and the wall-friction velocity $u_\tau = \sqrt{\tau_w/\rho}$ as characteristic length and velocity scales, respectively, where τ_w is the wall shear stress averaged over time and horizontal plane and ρ is the fluid density. The Reynolds number is defined as $Re_\tau = u_\tau h/\nu$, where ν is the kinematic viscosity. In the framework of resolvent analysis, the nonlinear term $-(\boldsymbol{u} \cdot \nabla)\,\boldsymbol{u}$ in Eq. (2) is treated as an external forcing, and the Reynolds stress term $\langle (\boldsymbol{u} \cdot \nabla)\,\boldsymbol{u} \rangle$ is approximated as [29]

$$\langle (\boldsymbol{u} \cdot \nabla)\,\boldsymbol{u} \rangle = \frac{1}{Re_\tau}\nabla \cdot \left[\frac{\nu_e}{\nu}\left(\nabla \boldsymbol{u} + \nabla \boldsymbol{u}^{\mathrm{T}}\right)\right], \tag{3}$$

where the eddy viscosity ν_e is given by the semi-empirical Cess model as [37]

$$\nu_e = \frac{\nu}{2}\sqrt{1 + \frac{\kappa^2 Re_\tau^2}{9}\left(1 - y^2\right)^2\left(1 + 2y^2\right)^2\left(1 - \mathrm{e}^{-y^+/A}\right)^2} - \frac{\nu}{2}. \tag{4}$$

The Kármán constant κ and constant A are set to 0.426 and 25.4 following del Álamo and Jiménez [20]. The dimensionless wall-normal coordinate y ranges from -1 to 1, and the wall coordinate is defined as $y^+ = Re_\tau\,(1 - |y|)$. Eq. (2) is then rewritten as

$$\frac{\partial \boldsymbol{u}}{\partial t} + (\boldsymbol{u} \cdot \nabla)\,\boldsymbol{U} + (\boldsymbol{U} \cdot \nabla)\,\boldsymbol{u} + \nabla p - \frac{1}{Re_\tau}\nabla \cdot \left[\frac{\nu_T}{\nu}\left(\nabla \boldsymbol{u} + \nabla \boldsymbol{u}^{\mathrm{T}}\right)\right] = \boldsymbol{f}, \tag{5}$$

where $\nu_T = \nu_e + \nu$ is the total viscosity, and $\boldsymbol{f} = -(\boldsymbol{u} \cdot \nabla)\,\boldsymbol{u}$ is treated as a forcing term in the resolvent analysis. To ensure the momentum conservation, the mean streamwise velocity at an arbitrary wall-normal location y is calculated by integrating $-Re_\tau \cdot y\nu/\nu_T$ from wall to y [35].

Assuming that the fully developed turbulent channel flow is statistically stationary in time and homogeneous in the wall-parallel directions, Fourier transform in time and in the streamwise and spanwise directions can be applied to an arbitrary field variable φ as

$$\hat{\varphi}(k_x, k_z, \omega; y) = \frac{1}{L_x L_z T}\int_0^{L_x}\int_0^{L_z}\int_0^{T} \mathrm{d}x\mathrm{d}z\mathrm{d}t \times w(t)\varphi(x, z, t; y)\exp[-\mathrm{i}(k_x x + k_z z - \omega t)], \tag{6}$$

where the variable with a hat $\hat{\varphi}$ represents the Fourier coefficient of φ, $w(t)$ is the window function in the time domain, L_x and L_z are the domain sizes in the $x-$ and $z-$directions, respectively, T is the time window length, $k_x = 2\pi m_x/L_x$ and $k_z = 2\pi m_z/L_z$ are wavenumbers in the $x-$ and $z-$directions, respectively, $\omega = 2\pi l/T$ is the frequency, m_x, m_z and l are integers, and $\mathrm{i} = \sqrt{-1}$ is the imaginary unit. Applying the Fourier transform given by Eq. (6) to the continuity and momentum equations, i.e., Eqs. (1) and (5), results in the following governing equations of $\hat{\boldsymbol{u}}$ in the Fourier space:

$$\hat{\nabla} \cdot \hat{u} = 0, \tag{7}$$

$$-i\omega\hat{\boldsymbol{u}} + \left(\hat{\boldsymbol{u}} \cdot \hat{\nabla}\right)\boldsymbol{U} + \left(\boldsymbol{U} \cdot \hat{\nabla}\right)\hat{\boldsymbol{u}} + \hat{\nabla}\hat{p} - \frac{1}{Re_\tau}\hat{\nabla} \cdot \left[\frac{\nu_T}{\nu}\left(\hat{\nabla}\hat{\boldsymbol{u}} + \hat{\nabla}\hat{\boldsymbol{u}}^{\mathrm{T}}\right)\right] = \hat{\boldsymbol{f}}, \tag{8}$$

where $\hat{\nabla} = \left[\mathrm{i}k_x, \partial/\partial y, \mathrm{i}k_z\right]^{\mathrm{T}}$ is the gradient operator in the Fourier space. Eqs. (7) and (8) can be re-arranged to obtain the following input–output relationship between the nonlinear forcing $\hat{\boldsymbol{f}}$ and the primitive state variable $\hat{\boldsymbol{q}}$:

$$\hat{\boldsymbol{q}} = \begin{bmatrix} \hat{\boldsymbol{u}} \\ \hat{p} \end{bmatrix} = \underbrace{\left(-\mathrm{i}\omega\begin{bmatrix} \boldsymbol{I} & 0 \end{bmatrix} - \begin{bmatrix} \boldsymbol{L} & -\hat{\nabla} \\ -\hat{\nabla}^{\mathrm{T}} & 0 \end{bmatrix}\right)^{-1}}_{H}\underbrace{\begin{bmatrix} \boldsymbol{I} \\ 0 \end{bmatrix}}_{B}\hat{\boldsymbol{f}} = \boldsymbol{H} \cdot \boldsymbol{B} \cdot \hat{\boldsymbol{f}} = \boldsymbol{R} \cdot \hat{\boldsymbol{f}}, \tag{9}$$

where $\hat{\boldsymbol{q}} = \left[\hat{u}, \hat{v}, \hat{w}, \hat{p}\right]^{\mathrm{T}}$ is employed to include pressure explicitly, $\boldsymbol{R}$ is the resolvent operator, $\boldsymbol{I}$ is a unit matrix, and $\boldsymbol{L}$ is the eddy-viscosity-enhanced linearized Navier–Stokes operator [38], defined as

$$\boldsymbol{L}=\begin{bmatrix} -\mathrm{i}k_x U+\frac{\nu_T}{\nu}\frac{\hat{\nabla}^2}{Re_\tau}+\frac{1}{Re_\tau}\frac{\mathrm{d}\nu_T}{\nu\mathrm{d}y}\frac{\partial}{\partial y} & -\frac{\mathrm{d}U}{\mathrm{d}y}+\frac{\mathrm{i}k_x}{Re_\tau}\frac{\mathrm{d}\nu_T}{\nu\mathrm{d}y} & 0 \\ 0 & -\mathrm{i}k_x U+\frac{\nu_T}{\nu}\frac{\hat{\nabla}^2}{Re_\tau}+\frac{2}{Re_\tau}\frac{\mathrm{d}\nu_T}{\nu\mathrm{d}y}\frac{\partial}{\partial y} & 0 \\ 0 & \frac{\mathrm{i}k_z}{Re_\tau}\frac{\mathrm{d}\nu_T}{\nu\mathrm{d}y} & -\mathrm{i}k_x U+\frac{\nu_T}{\nu}\frac{\hat{\nabla}^2}{Re_\tau}+\frac{1}{Re_\tau}\frac{\mathrm{d}\nu_T}{\nu\mathrm{d}y}\frac{\partial}{\partial y} \end{bmatrix}, \tag{10}$$

where $\hat{\nabla}^2=\partial^2/\partial y^2-k_x^2-k_z^2$ is the Laplace operator in the Fourier space. Operator $\boldsymbol{B}$ is used to enforce the right hand side of the continuity equation to be zero, which takes the following form

$$\boldsymbol{B}=\begin{bmatrix}\boldsymbol{I}\\ \boldsymbol{0}\end{bmatrix}=\begin{bmatrix}1&0&0\\0&1&0\\0&0&1\\0&0&0\end{bmatrix}. \tag{11}$$

The no-slip and no-penetration boundary conditions are adopted for the velocities at the wall, i.e.,

$$u=v=w=0 \quad \text{at} \quad y=\pm 1. \tag{12}$$

The boundary condition corresponding to the continuity equation can be the divergence-free condition at the wall, i.e.,

$$\frac{\partial v}{\partial y}=0 \quad \text{at} \quad y=\pm 1, \tag{13}$$

or the wall-normal momentum equation at the wall, i.e.,

$$-\frac{\partial p}{\partial y}+\frac{1}{Re_\tau}\frac{\partial^2 v}{\partial y^2}=0 \quad \text{at} \quad y=\pm 1. \tag{14}$$

Equation (13) ensures that the velocity field is divergence-free at any location in the computational domain, including the wall. The pressure is regarded as a passive quantity. This approach for implementing the pressure boundary condition is similar to the one used by McKeon and Sharma [28]. They projected the Navier–Stokes equations onto a group of divergence-free basis functions that satisfy the no-slip and no-penetration conditions at the wall. The pressure is as such eliminated in their formulas. Equation (14) is similar to the boundary condition used for solving the pressure Poisson equation, where the wall-normal momentum equation is kept to give a Neumann boundary condition for pressure at the wall. The effect of the boundary condition corresponding to the continuity equation on the predictive performance of the model is presented in Sect. 4.2. Resolvent analysis has been successfully applied to explain the formation of hairpin vortices [39], study the optimal growth of coherent streaks [30,31,33,34], model the dynamics of idealized turbulent bursting event [35], estimate large-scale structures [36], and analyze the convective velocities [40]. The statistical interpretation of resolvent analysis can be found in Ref. [41].

It is also effective to use resolvent analysis [to be specific, use Eq. (9)] to construct a predictive model of space–time energy spectra since its output is the velocity and pressure fluctuations in the Fourier space. As indicated by Eq. (9), the input forcing $\hat{\boldsymbol{f}}$ is mapped to the output state variable $\hat{\boldsymbol{q}}$ by the resolvent operator $\boldsymbol{R}$. In the literature, the resolvent analyses [28–35] focus on the properties of the resolvent operator $\boldsymbol{R}$, while $\hat{\boldsymbol{f}}$ is modeled as a harmonic, impulsive, or broadband stochastic forcing. However, to develop a predictive model for the space–time energy spectra, it is also crucial to give a precise forcing $\hat{\boldsymbol{f}}$. Moarref et al. [42] and Zare et al. [26] use a convex optimization method to model $\hat{\boldsymbol{f}}$ in the resolvent formula, which further results in the predictive model of the spatial energy spectra. More relevant to the present research, Towne et al. [27] develops the RBE method for the prediction of the space energy spectra, which approximates the space–time spectra of $\hat{\boldsymbol{f}}$ using the known space–time energy spectra at a reference wall-normal location. Compared to [26,42], the method of Towne et al. [27] avoids the complex convex optimization algorithm. In Sect. 2.2., we provide the detail equations for the numerical implementation of the RBE method.

2.2 Numerical implementation of the RBE method for space-time energy spectra

For numerical implementation, we first derive the discrete form of the resolvent operator $\hat{\boldsymbol{R}}$, state variable $\hat{\boldsymbol{q}}$ and nonlinear forcing $\hat{\boldsymbol{f}}$. Let $\hat{\boldsymbol{q}}_d=[\hat{u}_0,\hat{v}_0,\hat{w}_0,\hat{p}_0,\hat{u}_1,\hat{v}_1,\hat{w}_1,\hat{p}_1,\ldots,\hat{u}_N,\hat{v}_N,\hat{w}_N,\hat{p}_N]^{\mathrm{T}}\in\mathbb{C}^{4N+4}$ be the discrete state variable, where the subscript d represents variables after wall-normal discretization, $\mathbb{C}$ represents a set of complex matrices. As denoted using point A in Fig. 1, the RBE method needs the space–time spectra tensor known at a specific y-location as the input. This y-location is also called the reference plane in this paper.

Assuming that the reference plane is located at the kth discrete point, the subset of state variable $\hat{\boldsymbol{\theta}}_d$ at this point is related to the full set of discrete state variable $\hat{\boldsymbol{q}}_d$ as

$$\hat{\boldsymbol{\theta}}_d=[\hat{u}_k,\hat{v}_k,\hat{w}_k]^{\mathrm{T}}=\boldsymbol{C}\hat{\boldsymbol{q}}_d, \tag{15}$$

where $\boldsymbol{C} \in \mathbb{C}^{3\times(4N+4)}$ is a linear operator, expressed as

$$\boldsymbol{C} = \begin{bmatrix} \ddots & & 1 & & \ddots & \\ & 0 & & 1 & & 0 & \\ & & \ddots & \underbrace{1}_{(4k+1)-(4k+3)} & & \ddots & \end{bmatrix}. \tag{16}$$

Columns $(4k+1)$–$(4k+3)$ of $\boldsymbol{C}$ form a unit matrix, while other entries of $\boldsymbol{C}$ are zero. It should be noted that the components of $\hat{\boldsymbol{\theta}}_d$ are not limited to the velocities. The pressure can also be involved. The influence of the inclusion of pressure in $\hat{\boldsymbol{\theta}}_d$ is discussed in Sect. 4.3.

In the RBE method, the space–time spectra tensor $\boldsymbol{S}_{\theta\theta}(k_x, k_z, \omega)$ at the reference plane is needed as the input, which is defined as

$$\boldsymbol{S}_{\theta\theta}(k_x, k_z, \omega) = \left\langle \hat{\boldsymbol{\theta}}_d \hat{\boldsymbol{\theta}}_d^* \right\rangle \in \mathbb{C}^{3\times3}, \tag{17}$$

where the superscript "*" denotes a Hermitian transpose. The aim of the RBE method is to predict the following full spectra tensor of $\hat{\boldsymbol{q}}_d$

$$\boldsymbol{S}_{qq}(k_x, k_z, \omega) = \left\langle \hat{\boldsymbol{q}}_d \hat{\boldsymbol{q}}_d^* \right\rangle \in \mathbb{C}^{(4N+4)\times(4N+4)}. \tag{18}$$

To derive the prediction model of $\boldsymbol{S}_{qq}$, we start with the following discrete form of Eq. (9)

$$\hat{\boldsymbol{q}}_d = \boldsymbol{H}_q \boldsymbol{B}_q \hat{\boldsymbol{f}}_d = \boldsymbol{R}_q \hat{\boldsymbol{f}}_d, \tag{19}$$

where $\boldsymbol{R}_q \in \mathbb{C}^{(4N+4)\times(3N-3)}$ is the discrete resolvent operator, and $\boldsymbol{H}_q \in \mathbb{C}^{(4N+4)\times(4N+4)}$ and $\boldsymbol{B}_q \in \mathbb{C}^{(4N+4)\times(3N-3)}$ are the discrete form of $\boldsymbol{H}$ and $\boldsymbol{B}$ in Eq. (9).

The matrix $\boldsymbol{H}_q$ can be written as the summation of two parts as

$$\boldsymbol{H}_q = \boldsymbol{H}_d + \boldsymbol{H}_{nd}. \tag{20}$$

The first term $\boldsymbol{H}_d$ is a quasi-diagonal matrix, which includes all the terms in $\boldsymbol{H}_q$ except for wall-normal derivatives, viz.

$$\boldsymbol{H}_d = diag\left\{\boldsymbol{H}_{d;0}, ..., \boldsymbol{H}_{d;n}, ..., \boldsymbol{H}_{d;N}\right\} \in \mathbb{C}^{(4N+4)\times(4N+4)}, \tag{21}$$

where $diag\{\cdot\}$ denotes a quasi-diagonal matrix composed of the blocks in the brace, and $\boldsymbol{H}_{d;n}$ is expressed as

$$\boldsymbol{H}_{d;n} = \begin{bmatrix} -\mathrm{i}\omega + \mathrm{i}k_x U_n + \frac{\nu_{T,n}\left(k_x^2+k_z^2\right)}{\nu \cdot Re_\tau} & \frac{\mathrm{d}U_n}{\mathrm{d}y} - \frac{\mathrm{i}k_x}{Re_\tau}\frac{\mathrm{d}\nu_{T,n}}{\nu \mathrm{d}y} & 0 & \mathrm{i}k_x \\ 0 & -\mathrm{i}\omega + \mathrm{i}k_x U_n + \frac{\nu_{T,n}\left(k_x^2+k_z^2\right)}{\nu \cdot Re_\tau} & 0 & 0 \\ 0 & -\frac{\mathrm{i}k_z}{Re_\tau}\frac{\mathrm{d}\nu_{T,n}}{\nu \mathrm{d}y} & -\mathrm{i}\omega + \mathrm{i}k_x U_n + \frac{\nu_{T,n}\left(k_x^2+k_z^2\right)}{\nu \cdot Re_\tau} & \mathrm{i}k_z \\ \mathrm{i}k_x & 0 & \mathrm{i}k_z & 0 \end{bmatrix}, \tag{22}$$

where U_n, $\nu_{T,n}$, $\mathrm{d}U_n/\mathrm{d}y$, $\mathrm{d}\nu_{T,n}/\mathrm{d}y$ are the values of U, ν_T, $\mathrm{d}U/\mathrm{d}y$, $\mathrm{d}\nu_T/\mathrm{d}y$ at the nth discrete point, respectively. The second term $\boldsymbol{H}_{nd}$ in Eq. (20) includes the rest wall-normal derivative terms and can be written as

$$\boldsymbol{H}_{nd} = \begin{bmatrix} \boldsymbol{H}_{nd;0} \\ \vdots \\ \boldsymbol{H}_{nd;n} \\ \vdots \\ \boldsymbol{H}_{nd;N} \end{bmatrix} \in \mathbb{C}^{(4N+4)\times(4N+4)}, \tag{23}$$

where

$$\boldsymbol{H}_{nd,n} = \left[\boldsymbol{H}_{nd,n,0}, ..., \boldsymbol{H}_{nd,n,m}, ..., \boldsymbol{H}_{nd,n,N}\right] \in \mathbb{C}^{4\times(4N+4)}. \tag{24}$$

The component $\boldsymbol{H}_{nd;n,m}$ is expressed as

$$\boldsymbol{H}_{nd;n,m} = \begin{bmatrix} -\frac{\nu_{T,n}M_{2;n,m}}{\nu \cdot Re_\tau} - \frac{M_{1;n,m}}{Re_\tau}\frac{\mathrm{d}\nu_{T,n}}{\nu \mathrm{d}y} & 0 & 0 & 0 \\ 0 & -\frac{\nu_{T,n}M_{2;n,m}}{\nu \cdot Re_\tau} - \frac{2M_{1;n,m}}{Re_\tau}\frac{\mathrm{d}\nu_{T,n}}{\nu \mathrm{d}y} & 0 & M_{1;n,m} \\ 0 & 0 & -\frac{\nu_{T,n}M_{2;n,m}}{\nu \cdot Re_\tau} - \frac{M_{1;n,m}}{Re_\tau}\frac{\mathrm{d}\nu_{T,n}}{\nu \mathrm{d}y} & 0 \\ 0 & M_{1;n,m} & 0 & 0 \end{bmatrix}, \tag{25}$$

where $\boldsymbol{M}_1 = \left[M_{1;n,m}\right] \in \mathbb{R}^{(N+1)\times(N+1)}$ and $\boldsymbol{M}_2 = \left[M_{2;n,m}\right] \in \mathbb{R}^{(N+1)\times(N+1)}$ are the matrices for calculating the first and second-order derivatives in the wall-normal direction, and $\mathbb{R}$ represents a set of real matrices. In the present research, we follow Towne et al. [27] to discretize Eq. (9) at Chebyshev collocation points $y_n = \cos(n\pi/N)$. The detailed forms of

$\boldsymbol{M}_1$ and $\boldsymbol{M}_2$ can be found in Trefenthen [43]. To incorporate the boundary condition, $\boldsymbol{H}_{d;0}$, $\boldsymbol{H}_{d;N}$, $\boldsymbol{H}_{nd;0}$ and $\boldsymbol{H}_{nd;N}$ in Eqs. (21) and (23) need to be modified. The details are given in Sect. 4.2.

The matrix $\boldsymbol{B}_q$ in Eq. (19) is expressed as

$$\boldsymbol{B}_q = \begin{bmatrix} \boldsymbol{B}_u \\ \boldsymbol{B}_{mid} \\ \boldsymbol{B}_d \end{bmatrix} \in \mathbb{R}^{(4N+4)\times(3N-3)}, \tag{26}$$

where $\boldsymbol{B}_u = \boldsymbol{B}_d = \boldsymbol{0} \in \mathbb{R}^{4\times(3N-3)}$, and $\boldsymbol{B}_{mid} = diag\{\boldsymbol{B}_1, ..., \boldsymbol{B}_n, ..., \boldsymbol{B}_{N-1}\} \in \mathbb{R}^{(4N-4)\times(3N-3)}$ is a quasi-diagonal matrix, with

$$\boldsymbol{B}_n = \begin{bmatrix} 1 & 0 & 0 \\ 0 & 1 & 0 \\ 0 & 0 & 1 \\ 0 & 0 & 0 \end{bmatrix}, n = 1, 2, ..., N-1. \tag{27}$$

The zero matrices $\boldsymbol{B}_u$ and $\boldsymbol{B}_d$ appear because there is no forcing in the boundary conditions given by Eqs. (12)–(14).

So far, the discrete forms of matrices $\boldsymbol{H}_q$ and $\boldsymbol{B}_q$ are given, and thus according to Eq. (19), $\hat{\boldsymbol{q}}_d$ is obtained if $\hat{\boldsymbol{f}}_d$ is known. Therefore, to develop the predictive model of the space–time spectra tensor of $\hat{\boldsymbol{q}}_d$, the key process is to connect $\hat{\boldsymbol{f}}_d$ with $\hat{\boldsymbol{\theta}}_d$. To this purpose, the matrix $\boldsymbol{C}$ given by Eq. (16) is multiplied to Eq. (19) to yield

$$\hat{\boldsymbol{\theta}}_d = \boldsymbol{R}_\theta \hat{\boldsymbol{f}}_d, \tag{28}$$

where $\boldsymbol{R}_\theta = \boldsymbol{C}\boldsymbol{R}_q \in \mathbb{C}^{3\times(3N-3)}$ is a localized resolvent operator at the reference plane. Substituting Eqs. (19) and (28) into Eqs. (18) and (17), respectively, results in the following relationships

$$\boldsymbol{S}_{qq} = \left\langle \hat{\boldsymbol{q}}_d \hat{\boldsymbol{q}}_d^* \right\rangle = \boldsymbol{R}_q \boldsymbol{S}_{ff} \boldsymbol{R}_q^* \in \mathbb{C}^{(4N+4)\times(4N+4)}, \tag{29}$$

$$\boldsymbol{S}_{\theta\theta} = \left\langle \hat{\boldsymbol{\theta}}_d \hat{\boldsymbol{\theta}}_d^* \right\rangle = \boldsymbol{R}_\theta \boldsymbol{S}_{ff} \boldsymbol{R}_\theta^* \in \mathbb{C}^{3\times3}, \tag{30}$$

where $\boldsymbol{S}_{ff} = \left\langle \hat{\boldsymbol{f}}_d \hat{\boldsymbol{f}}_d^* \right\rangle \in \mathbb{C}^{(3N-3)\times(3N-3)}$ is the space–time spectra tensor of $\hat{\boldsymbol{f}}_d$. Eq. (29) shows that $\boldsymbol{S}_{qq}$ can be calculated if $\boldsymbol{S}_{ff}$ is given. To obtain $\boldsymbol{S}_{ff}$ based on the given $\boldsymbol{S}_{\theta\theta}$, the singular value decomposition (SVD) of the localized resolvent operator $\boldsymbol{R}_\theta$ is conducted as

$$\boldsymbol{R}_\theta = \boldsymbol{U}_\theta \boldsymbol{\Sigma}_\theta \boldsymbol{V}_\theta^*, \tag{31}$$

where $\boldsymbol{U}_\theta \in \mathbb{C}^{3\times3}$, $\boldsymbol{\Sigma}_\theta \in \mathbb{C}^{3\times(3N-3)}$ and $\boldsymbol{V}_\theta \in \mathbb{C}^{(3N-3)\times(3N-3)}$ are response modes (output resolvent modes), singular value matrix, and forcing modes (input resolvent modes), respectively. To simplify the mathematical representation, matrices $\boldsymbol{\Sigma}_\theta$ and $\boldsymbol{V}_\theta$ are written in a block form following Towne et al. [27] as

$$\boldsymbol{\Sigma}_\theta = \begin{bmatrix} \boldsymbol{\Sigma}_1 & \boldsymbol{0} \end{bmatrix}, \tag{32}$$

$$\boldsymbol{V}_\theta^* = \begin{bmatrix} \boldsymbol{V}_1 & \boldsymbol{V}_2 \end{bmatrix}^*, \tag{33}$$

where $\boldsymbol{\Sigma}_1 \in \mathbb{R}^{3\times3}$ is the diagonal singular value matrix, $\boldsymbol{V}_1 \in \mathbb{C}^{(3N-3)\times3}$ and $\boldsymbol{V}_2 \in \mathbb{C}^{(3N-3)\times(3N-6)}$ are forcing modes that have non-zero and zero responses, respectively.

The forcing modes $\boldsymbol{V}_\theta$ are the orthogonal basis of $\hat{\boldsymbol{f}}_d$, while the response modes are the orthogonal bases of the output state variable $\hat{\boldsymbol{\theta}}_d$. The forcing $\hat{\boldsymbol{f}}_d$ is then projected as

$$\hat{\boldsymbol{f}}_d = \boldsymbol{V}_\theta \boldsymbol{e}, \tag{34}$$

where $\boldsymbol{e} \in \mathbb{C}^{3N-3}$ is the expansion coefficients vector of $\hat{\boldsymbol{f}}_d$. Multiplying Eq. (34) with its Hermitian transpose, and taking ensemble averaging yields the following expansion of $\boldsymbol{S}_{ff}$ on the forcing modes

$$\boldsymbol{S}_{ff} = \begin{bmatrix} \boldsymbol{V}_1 & \boldsymbol{V}_2 \end{bmatrix} \begin{bmatrix} \boldsymbol{E}_{11} & \boldsymbol{E}_{12} \\ \boldsymbol{E}_{21} & \boldsymbol{E}_{22} \end{bmatrix} \begin{bmatrix} \boldsymbol{V}_1 & \boldsymbol{V}_2 \end{bmatrix}^*, \tag{35}$$

where $\boldsymbol{E}_{ij}$ are coefficient matrices. Note that the degree of freedom of $\boldsymbol{S}_{ff}$ is larger than that of $\boldsymbol{S}_{\theta\theta}$. This spectra-estimation problem is thus undetermined. If it is required that the space–time energy spectra at the reference plane are recovered exactly, the coefficient matrix $\boldsymbol{E}_{11}$ is determined by substituting Eq. (35) into Eq. (30) as

$$\boldsymbol{E}_{11} = \boldsymbol{\Sigma}_1^{-1} \boldsymbol{U}_\theta^* \boldsymbol{S}_{\theta\theta} \boldsymbol{U}_\theta \boldsymbol{\Sigma}_1^{-1}. \tag{36}$$

In the method of Towne et al. [27], it is assumed that the nonlinear forcing only has non-zero expansion coefficients on $\boldsymbol{V}_1$, and as a result $\boldsymbol{E}_{12} = \boldsymbol{E}_{21} = \boldsymbol{E}_{22} = \boldsymbol{0}$ holds. It is proved that this approximation is equivalent to taking the least squares approximation of $\boldsymbol{S}_{ff}$ [27]. Substituting Eq. (36) into Eq. (35) and setting other coefficient matrices zero yields

$$\boldsymbol{S}_{ff} = \boldsymbol{V}_1 \boldsymbol{\Sigma}_1^{-1} \boldsymbol{U}_\theta^* \boldsymbol{S}_{\theta\theta} \boldsymbol{U}_\theta \boldsymbol{\Sigma}_1^{-1} \boldsymbol{V}_1^*. \tag{37}$$

Finally, substituting Eq. (37) into Eq. (29) results in

$$\boldsymbol{S}_{qq} = \boldsymbol{R}_q \boldsymbol{V}_1 \boldsymbol{\Sigma}_1^{-1} \boldsymbol{U}_\theta^* \boldsymbol{S}_{\theta\theta} \boldsymbol{U}_\theta \boldsymbol{\Sigma}_1^{-1} \boldsymbol{V}_1^* \boldsymbol{R}_q^*. \tag{38}$$

Equation (38) gives the relationship between $\boldsymbol{S}_{\theta\theta}$ and $\boldsymbol{S}_{qq}$ in the RBE method. The $(4k+1)$–$(4k+3)$ diagonal elements in $\boldsymbol{S}_{qq}$ are the space–time energy spectra in three directions at the kth collocation point. The RMS velocity profiles then can be calculated as the summation of the space–time energy spectra over all wavenumbers and frequencies.

3 Numerical set-up and data processing

To carry out the numerically implement and evaluate the RBE method, direct numerical simulation (DNS) is conducted to obtain the data of turbulent channel flow at $Re_\tau = 187$. The flow is driven by a constant pressure gradient in the streamwise direction. The computational domain size is $L_x \times L_y \times L_z = 2\pi \times 2 \times \pi$, and the number of Fourier modes is 64 in both streamwise and spanwise directions, while 129 Chebyshev polynomials are used for the discretization in the wall-normal direction. The setting is kept identical to Towne et al. [27]. The DNS code has been well tested and used in Refs. [12,44,45]. The mean velocity and RMS velocities obtained from the present DNS agree with those of Moser et al. [46].

The flow fields are stored at 20000 time instances with the time separation between two storage time instances being $\Delta t^+ = 0.75$. To conduct Fourier transform in time, 512 successive time instances are grouped as a time window with 75% window overlap. The numerical setting ensures that the frequency resolution are in agreement with Ref. [27]. In each time window, the state variable is Fourier transformed in time to obtain the frequency modes. Since the flow quantities are not strictly periodic in time, the following standard Hanning window [47] is used in the Fourier transform

$$\hat{\boldsymbol{u}}(\boldsymbol{x},\omega) = \frac{1}{\sqrt{T\int_0^T w_H^2(t)\mathrm{d}t}} \int_0^T w_H(t)\boldsymbol{u}(\boldsymbol{x},t)\exp(\mathrm{i}\omega t)\mathrm{d}t, \tag{39}$$

where $w_H(t)$ is the Hanning window, expressed as

$$w_H(t) = \frac{1}{2}\left[1+\cos\left(\frac{2\pi t}{T}-\pi\right)\right]. \tag{40}$$

Note that a rectangular window function is adopted by Towne et al. [27]. A detailed discussion about the window function is given in Sect. 4.4. The ensemble averaging is calculated by the averaging over all time windows. The energy spectra for $64 \times 64 \times 512$ wall-parallel wavenumbers and frequency combinations are estimated using the method introduced in Sect. 2. For a given wavenumber–frequency mode, the SVD and other computation of large-scale matrices are computed. Therefore, a total of about one million SVDs need to be conducted, which is time consuming. To speed-up the computation, we developed a parallelized FORTRAN code. Wavenumber–frequency combinations are divided into different groups to be processed on different CPU cores.

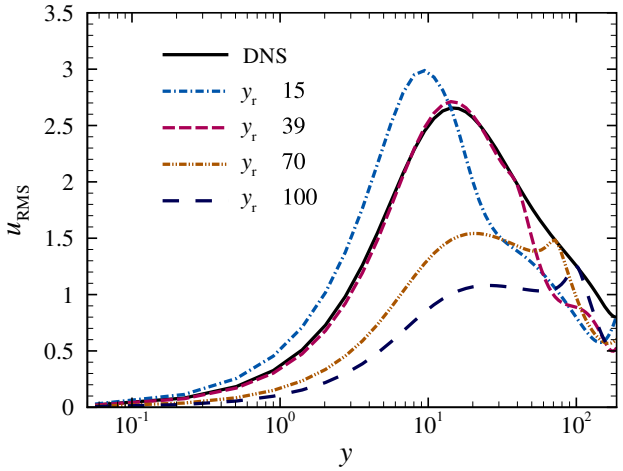

Fig. 2 Profiles of the streamwise RMS velocity u_{RMS} obtained from the RBE method for different wall-normal locations of the reference plane. The DNS result is shown for comparison

4 Numerical evaluation

4.1 Locations of reference planes

In this section, we study the effects of the location of the reference plane on the resolvent-based estimation. Figure 2 shows the predicted profiles of the streamwise RMS velocity u_{RMS} by setting the reference plane at $y_r^+ = 15$, 39, 70 and 100. The DNS profile is plotted for comparison. It is seen from the figure that when the reference plane is located at $y_r^+ = 39$, the profile of u_{RMS} obtained from the RBE method is in good agreement with the DNS result below the reference plane, while its magnitude is underestimated above the reference plane. This observation is consistent with Towne et al. [27]. However, if the reference plane is shifted to $y_r^+ = 15$, the magnitude of u_{RMS} obtained from the RBE method is over-predicted below $y_r^+ = 15$ and under-predicted above $y_r^+ = 15$. In the cases for $y_r^+ = 70$ and 100, the magnitude of u_{RMS} is under-predicted across the entire channel. The results of u_{RMS} shown in Fig. 2 indicate that the location of the reference plane influences the prediction of the streamwise RMS velocity.

Figure 3a, c compare the contours of space–time energy spectra $\Phi(k_x,\omega)$ at $y^+ = 15$ predicted by the RBE method based on two different reference planes ($y_r^+ = 39$ and 70, respectively) with the DNS results. To highlight the wavenumbers and frequencies with high energy levels, the contours corresponding to lower energy levels ($\Phi(k_x,\omega) < 10^{-9}$) are clipped. As shown in both Fig. 3a, c, the RBE method appropriately captures the Doppler shift and broadening of the space–time energy spectra caused by the convection and sweeping, respectively [17]. However, the bandwidths of the space–time energy spectra obtained from the RBE method are narrower than the DNS result. Further-

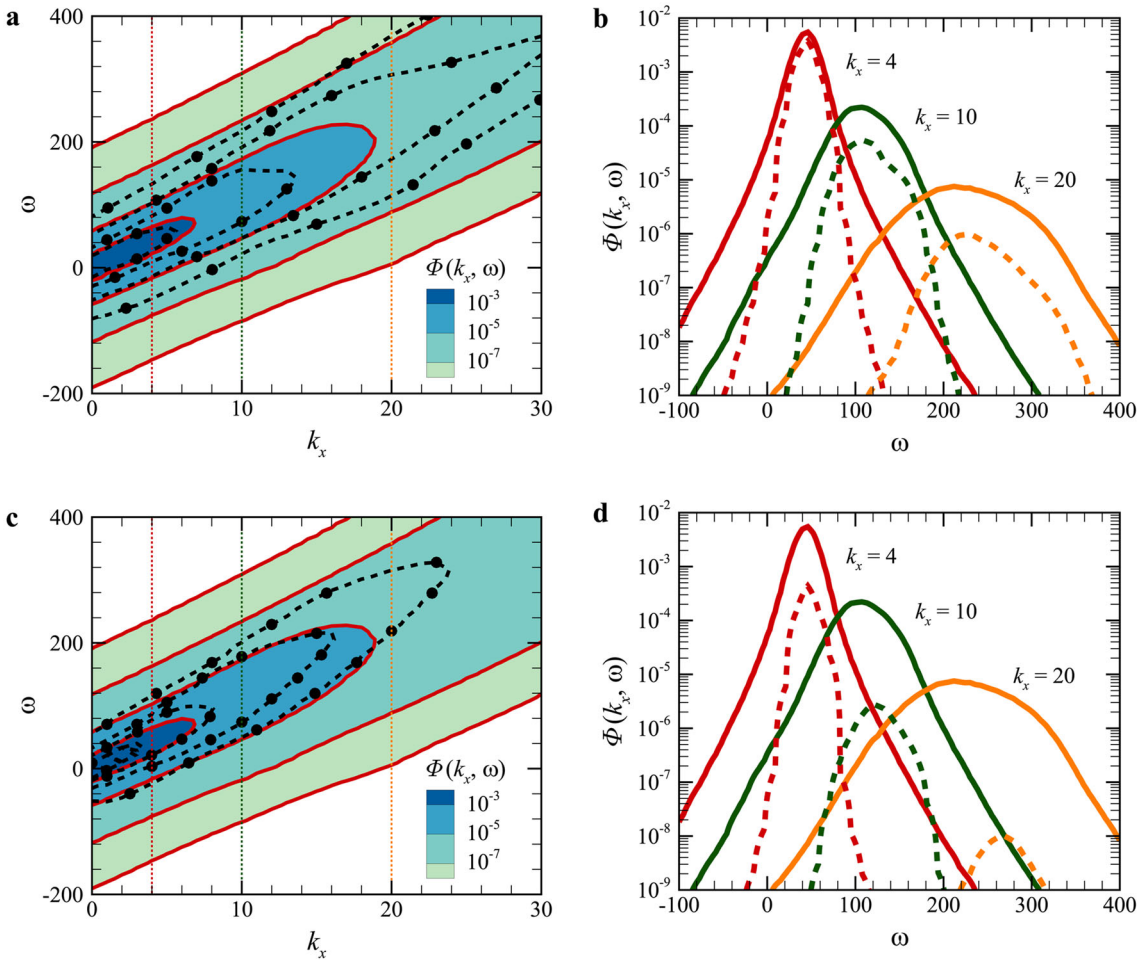

Fig. 3 Comparison of the space–time energy spectra at $y^+ = 15$ obtained from the RBE method and DNS. **a**, **c** show the contours of the space–time energy spectra obtained from the RBE method (dashed lines with dots) and DNS (color contours). **b**, **d** show the space–time energy spectra as a function of the frequency at three given wavenumbers, i.e., $k_x = 4$, 10, and 20, denoted using the vertical dotted lines in **a**, **c**, respectively. The results of the RBE method and DNS are shown using the dashed and solid lines, respectively. The reference plane is located at **a**, **b** $y_r^+ = 39$ and **c**, **d** $y_r^+ = 70$

more, from the comparison between Fig. 3a, b and c, d, it is seen that the spectral bandwidth for $y_r^+ = 70$ is narrower than that for $y_r^+ = 39$, especially at high wavenumbers. This indicates a less satisfactory performance of the RBE method by setting the reference plane at $y_r^+ = 70$ than at $y_r^+ = 39$, an observation that is consistent with the results of the streamwise RMS velocity shown in Fig. 2.

To facilitate a quantitative comparison of the space–time energy spectra obtained from the RBE method and DNS, we examine the wavenumber-dependent convection velocity $U_c(k_x)$ and spectral bandwidth $B(k_x)$ of $\Phi(k_x, \omega)$, defined as [12,13]

$$U_c(k_x) = \frac{\int \omega \cdot \Phi(k_x, \omega) \mathrm{d}\omega}{k_x \int \Phi(k_x, \omega) \mathrm{d}\omega}, \tag{41}$$

and

$$B(k_x) = \frac{\int (\omega - U_c(k_x)k_x)^2 \Phi(k_x, \omega) \mathrm{d}\omega}{\int \Phi(k_x, \omega) \mathrm{d}\omega}, \tag{42}$$

respectively. Figure 4a, b compares the values of $U_c(k_x)$ and $B(k_x)$ as functions of the streamwise wavenumber k_x obtained from the RBE method and DNS. The convection velocity $U_c(k_x)$ characterizes how the propagating speed of an eddy is related to its length scale [48]. It is observed from Fig. 4a that if the reference plane is set to $y_r^+ = 39$, the convection velocity of the RBE method is close to the DNS result. However, as the reference plane is shifted to $y_r^+ = 70$, the RBE method overestimates the value of $U_c(k_x)$ at all wavenumbers under investigation.

The bandwidth $B(k_x)$ is the standard variance of $\Phi(k_x, \omega)$, which characterizes to what extent the space–time energy spectra deviate from the Taylor's frozen flow hypothesis [49]. Figure 4b shows that the values of $B(k_x)$ for both $y_r^+ = 39$

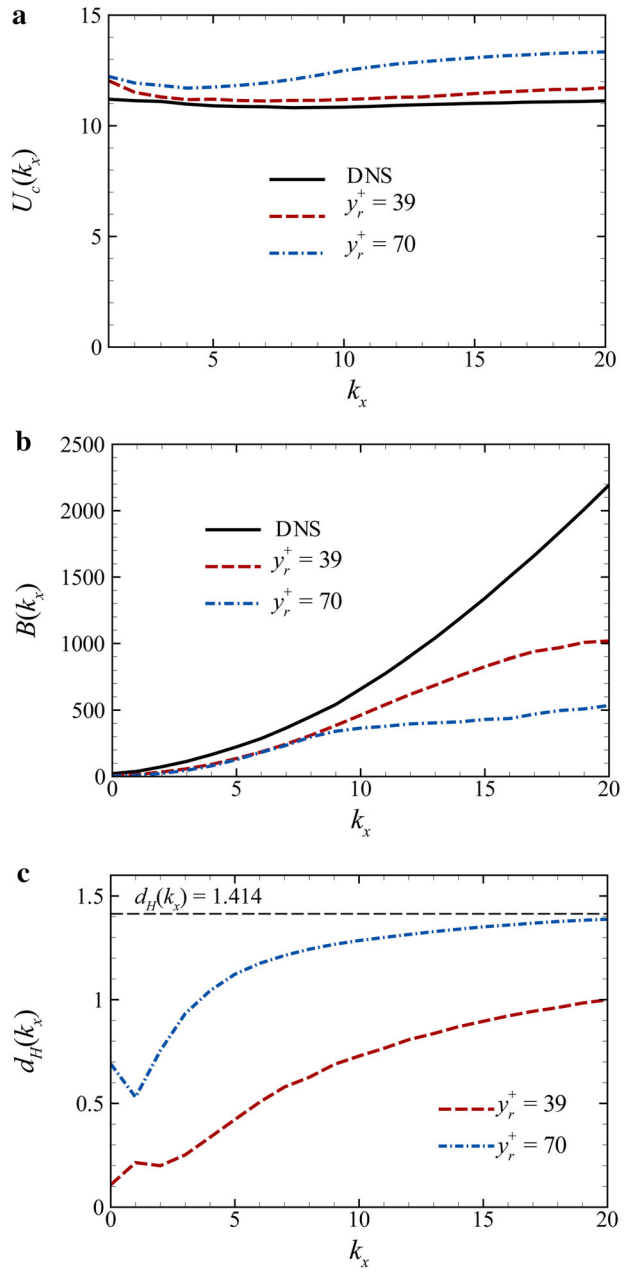

Fig. 4 Comparison of **a** the wavenumber-dependent convection velocity $U_c(k_x)$, **b** spectral bandwidth $B(k_x)$ and **c** Hellinger distance $d_H(k_x)$ of space–time energy spectra at $y^+ = 15$ obtained from the RBE method (with the reference plane located at $y_r^+ = 39$ and 70) and DNS

and $y_r^+ = 70$ are underestimated by the RBE method. At relatively low wavenumbers for $k_x < 8$, the results for $y_r^+ = 39$ and $y_r^+ = 70$ are close, but at larger wavenumbers, the result for $y_r^+ = 39$ is closer to the DNS result than that for $y_r^+ = 70$.

The performance of the RBE method in the prediction of the space–time energy spectra can be further quantified using the Hellinger distance [13,50] between the RBE and DNS results, defined as

$$d_H(k_x) = \sqrt{\frac{2\int\left(\sqrt{\Phi^{RBE}(k_x,\omega)} - \sqrt{\Phi^{DNS}(k_x,\omega)}\right)^2 \mathrm{d}\omega}{\Phi^{RBE}(k_x) + \Phi^{DNS}(k_x)}}. \tag{43}$$

where $\Phi(k_x)$ is the streamwise wavenumber spectrum. The value of the Hellinger distance equals to zero if and only if $\Phi^{DNS}(k_x,\omega) = \Phi^{RBE}(k_x,\omega)$ holds, while it reaches the maximum $\sqrt{2}$ when $\Phi^{DNS}(k_x,\omega)$ is significantly larger or smaller than $\Phi^{RBE}(k_x,\omega)$. Figure 4c compares the Hellinger distance at $y^+ = 15$ corresponding to $y_r^+ = 39$ and $y_r^+ = 70$. As shown, the value of the Hellinger distance for $y_r^+ = 39$ is smaller than that for $y_r^+ = 70$. Furthermore, the Hellinger distance increases with wavenumber, indicating a better performance of RBE at larger scales.

4.2 Pressure boundary conditions

In the numerical implementation of the resolvent analysis, the pressure boundary condition needs to be satisfied at each wall to close the equations. In general, there are two approaches given by Eqs. (13) and (14), respectively, for the incorporation of the pressure boundary condition. To implement Eq. (13), $\boldsymbol{H}_{d;0}$, $\boldsymbol{H}_{d;N}$, $\boldsymbol{H}_{nd;0}$, and $\boldsymbol{H}_{nd;N}$ in Eqs. (21–25) are modified as

$$\boldsymbol{H}_{d;0} = \boldsymbol{H}_{d;N} = diag\{1, 1, 1, 0\}, \tag{44}$$

$$\boldsymbol{H}_{nd;0,l} = \begin{bmatrix} 0 & 0 & 0\,0 \\ 0 & 0 & 0\,0 \\ 0 & 0 & 0\,0 \\ 0 & M_{1;0,l} & 0\,0 \end{bmatrix}, \tag{45a}$$

$$\boldsymbol{H}_{nd;N,l} = \begin{bmatrix} 0 & 0 & 0\,0 \\ 0 & 0 & 0\,0 \\ 0 & 0 & 0\,0 \\ 0 & M_{1;N,l} & 0\,0 \end{bmatrix}, l = 0, 1, ..., N. \tag{45b}$$

To implement the other pressure boundary condition given by Eq. (14), the diagonal part of $\boldsymbol{H}$ is also modified by Eq. (44), while the non-diagonal part is prescribed as

$$\boldsymbol{H}_{nd;0,l} = \begin{bmatrix} 0 & 0 & 0 & 0 \\ 0 & 0 & 0 & 0 \\ 0 & 0 & 0 & 0 \\ 0 & \frac{M_{2;0,l}}{Re_\tau} & 0 & -M_{1;0,l} \end{bmatrix}, \tag{46a}$$

$$\boldsymbol{H}_{nd;N,l} = \begin{bmatrix} 0 & 0 & 0 & 0 \\ 0 & 0 & 0 & 0 \\ 0 & 0 & 0 & 0 \\ 0 & \frac{M_{2;N,l}}{Re_\tau} & 0 & -M_{1;N,l} \end{bmatrix}, l = 0, 1, ..., N. \tag{46b}$$

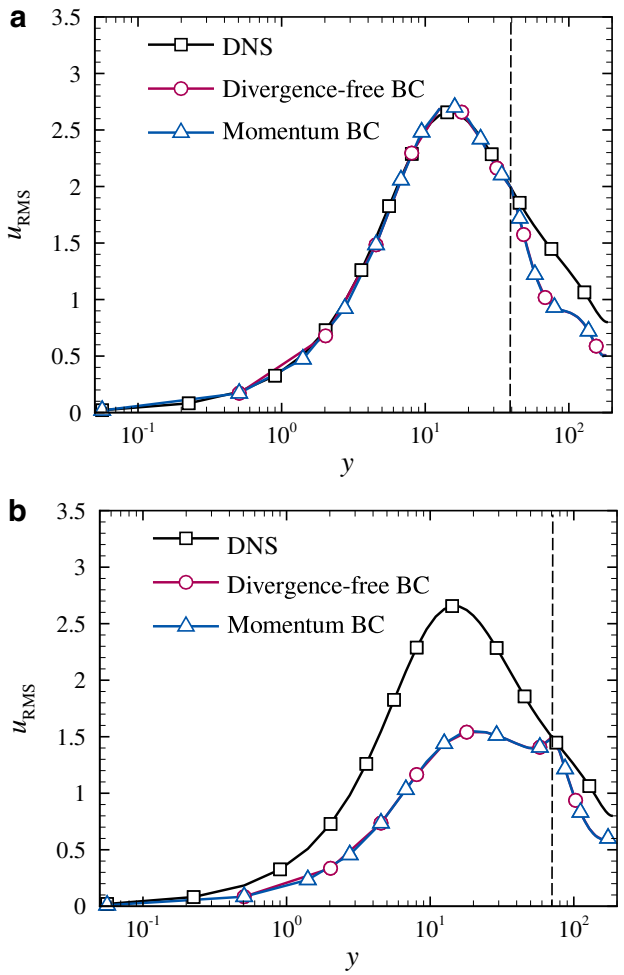

Fig. 5 Profiles of the streamwise RMS velocity u_{RMS} obtained from the RBE method based on different implementations of the pressure boundary condition. The DNS result is superimposed for comparison. The reference plane is located at **a** $y_r^+ = 39$ and **b** $y_r^+ = 70$. The location of the reference plane is demarcated using the vertical dashed line

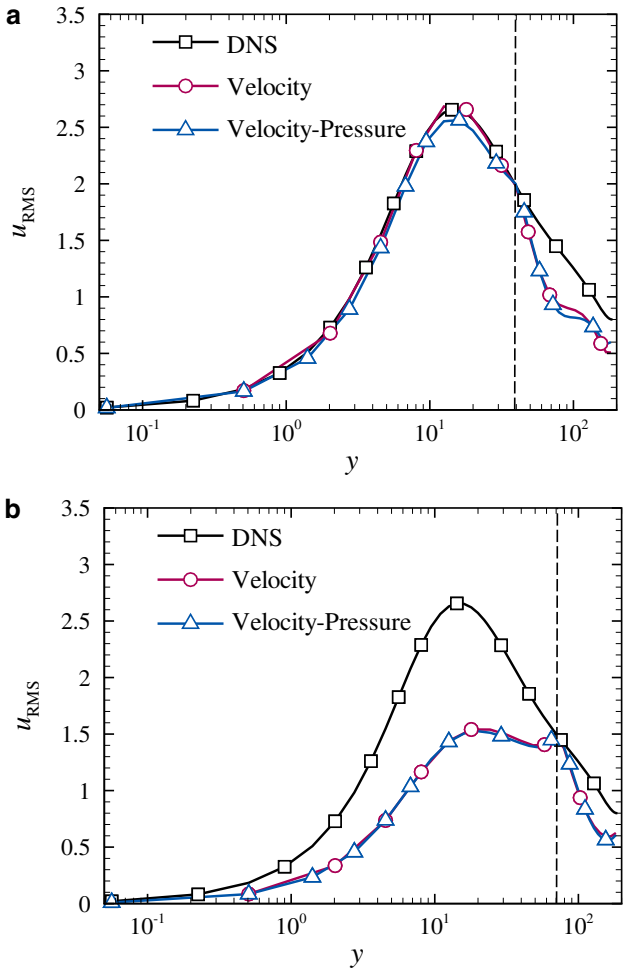

Fig. 6 Profiles of the streamwise RMS velocity u_{RMS} obtained from the RBE method with and without the inclusion of pressure as an input variable. The DNS result is superimposed for comparison. The reference plane is located at **a** $y_r^+ = 39$ and **b** $y_r^+ = 70$. The location of the reference plane is demarcated using the vertical dashed line

Figure 5 compares the profiles of u_{RMS} obtained from the RBE method based on different implementations of the pressure boundary condition. We have examined different locations of the reference plane, among which the results for $y_r^+ = 39$ and $y_r^+ = 70$ are depicted as representations. The DNS result is also shown for comparison. It is evident from Fig. 5 that the profiles of u_{RMS} based on the two different boundary conditions collapse. The examination results of the predicted space–time energy spectra are not shown to keep the paper concise. We found that the pressure boundary condition also imposes no influence on the predicted space–time energy spectra. The results shown in this section indicate that the two types of the pressure boundary condition are essentially equivalent in the RBE method.

4.3 Inclusion of pressure as an input

In above sections, the input local state variable $\hat{\boldsymbol{\theta}}_d$ consists of the three velocity components [Eq. (15)] following Towne et al. [27]. In this section, we further examine if the inclusion of pressure as an input variable influences the performance of the RBE method. To include the pressure as an input variable, the local state variable $\hat{\boldsymbol{\theta}}_d$ is modified as

$$\hat{\boldsymbol{\theta}}_d = [\hat{u}_k, \hat{v}_k, \hat{w}_k, \hat{p}_k]^{\mathrm{T}}. \tag{47}$$

Accordingly, the pressure spectra and velocity–pressure co-spectra are included in $\boldsymbol{S}_{\theta\theta}(k_x, k_z, \omega)$. The matrix $\boldsymbol{C}$ is then modified to

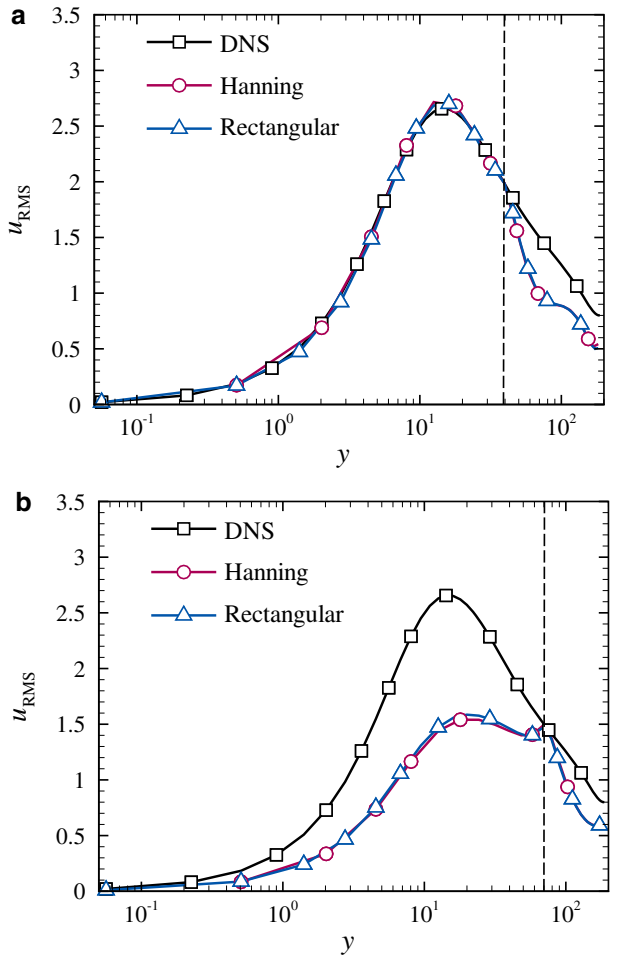

Fig. 7 Profiles of the streamwise RMS velocity u_{RMS} obtained from the RBE method using different window functions in time–frequency Fourier transform. The DNS result is superimposed for comparison. The reference plane is located at **a** $y_r^+ = 39$ and **b** $y_r^+ = 70$. The location of the reference plane is demarcated using the vertical dashed line

$$\boldsymbol{C} = \begin{bmatrix} \ddots & & 1 & & \ddots \\ & 0 & & 1 & & 0 & \\ & & 0 & & 1 & & 0 & \\ & & & \ddots & \underbrace{\quad 1 \quad}_{4k+1\sim 4k+4} & & \ddots \end{bmatrix} \in \mathbb{R}^{4\times(4N+4)}. \tag{48}$$

The procedure for predicting the space–time energy spectra given by Eqs. (15–38) remains the same, but the sizes of most matrices are changed, due to the change in the size of $\boldsymbol{C}$.

Figure 6 compares the predicted profiles of u_{RMS} with and without including pressure as an input variable. The results for $y_r^+ = 39$ and 70 are shown as representations. It is seen from both Figs. 6a and 6b that including pressure leads to little change in the profile of u_{RMS}^+ for both $y_r^+ = 39$ and $y_r^+ = 70$, respectively. The space–time energy spectra are also not influenced by the inclusion of the pressure as an input, which is not shown to keep the paper concise. The results shown in this section indicate that the pressure is to some extent "passive" in the RBE method. This conclusion also supports the approach of McKeon and Sharma [28] that projects the fluctuating velocities onto a set of divergence-free basis functions satisfying the no-slip and no-penetration conditions at the walls to eliminate the pressure in the resolvent operator.

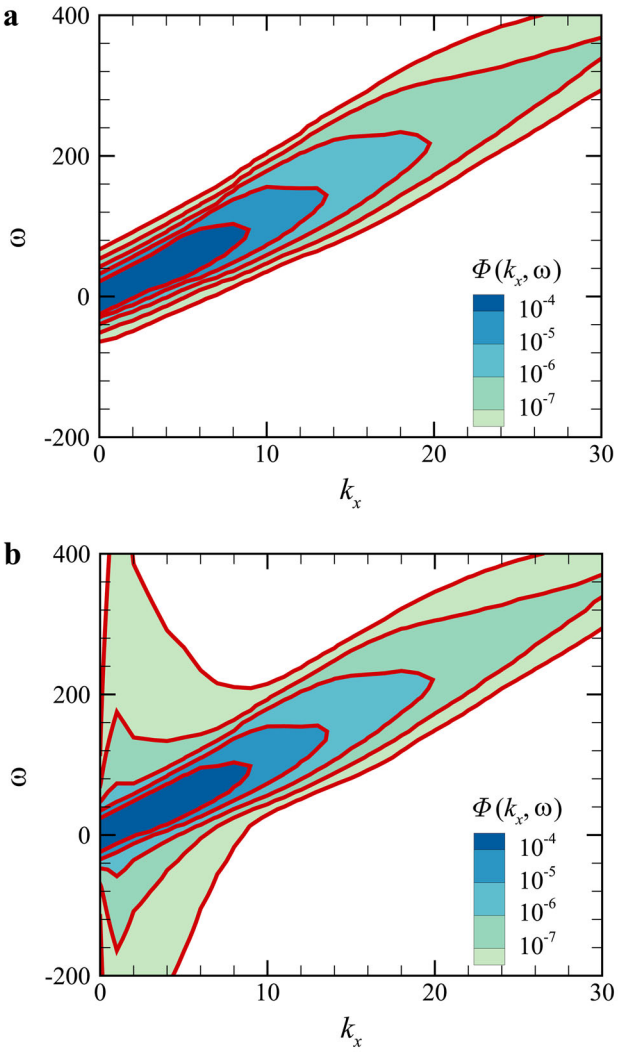

Fig. 8 Contours of the space–time energy spectra $\Phi(k_x, \omega)$ predicted by the RBE method at $y^+ = 15$ using **a** Hanning and **b** rectangular window functions in the time–frequency Fourier transform. The reference plane is located at $y_r^+ = 39$

4.4 Window function

In this section, the effects of the window function on the space–time energy spectra are investigated. The window function is introduced to calculate the space–time energy spectra because the velocity signal is not strictly periodic in

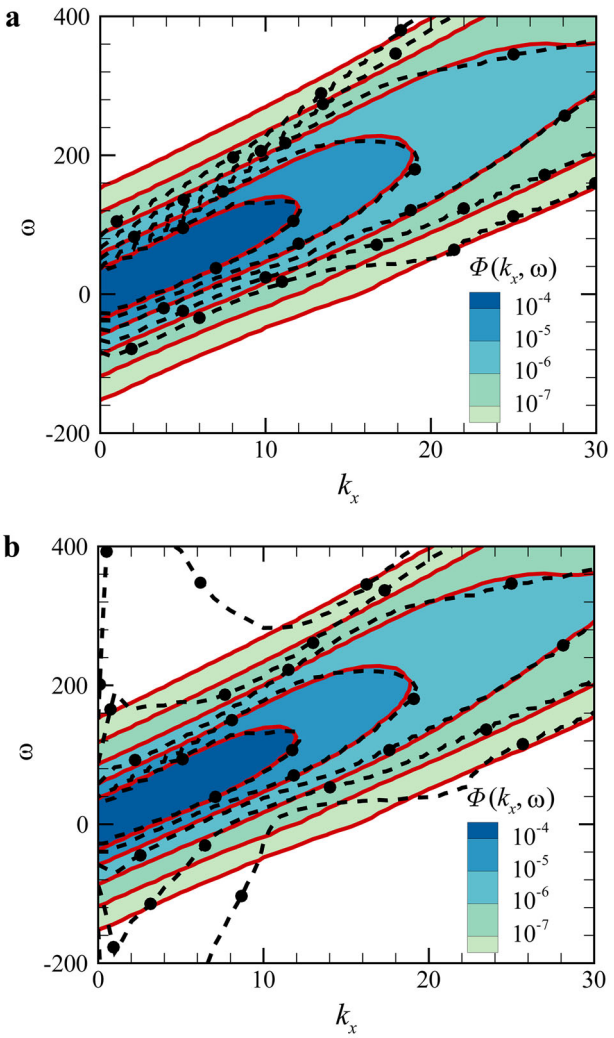

Fig. 9 Contours (dashed lines with dots) of the rescaled space–time energy spectra at $y^+ = 15$ obtained from the RBE method based on **a** Hanning window and **b** rectangular window. The DNS results are superimposed as the color contours with the solid lines for comparison. The reference plane is located at $y_r^+ = 39$

time. When the space–time energy spectra are calculated by processing the DNS data, a window function should be used to restrain the spectral leakage when the velocity signal is transformed from the time domain to the frequency domain.

Figure 7 compares the predicted profiles of streamwise RMS velocity u_{RMS} using the rectangular and Hanning window functions. The results for $y_r^+ = 39$ and $y_r^+ = 70$ as shown. It is seen that the window function imposes almost no influence on the predicted profiles. However, a further examination of the space–time energy spectra shows the effects of the window function.

Figure 8 compares the contours of the space–time energy spectra $\Phi(k_x, \omega)$ predicted by the RBE method at $y^+ = 15$ using different window functions in the time–frequency Fourier transform. It is seen that if the Hanning window is adopted, the predicted contours of $\Phi(k_x, \omega)$ are closed curves (Fig. 8a). However, if a rectangular window is used, the predicted contours are not closed (Fig. 8b). The spectral leakage can be observed in the frequency direction. At small streamwise wavenumbers for $k_x < 10$, the kinetic energy leaks from low frequencies to high frequencies. Therefore, although the predicted profiles of the streamwise RMS velocity are not influenced by the window function, the Hanning window can effectively reduce the spectral leakage in the space–time energy spectra.

To further demonstrate the effects of window functions on the prediction of space–time energy spectra using the RBE method, the space–time energy spectra obtained from the RBE method is rescaled using the technique proposed by Wu et al. [12], which uses the following linear transformation to ensure that the rescaled RBE spectra have the same energy, convection velocity, and spectral bandwidth as the DNS results:

$$\tilde{\omega} = \lambda_2(k_x)\omega + \lambda_3(k_x), \tag{49}$$

$$\tilde{\Phi}(k_x, \tilde{\omega}) = \frac{\lambda_1(k_x)}{\lambda_2(k_x)}\Phi(k_x, \omega), \tag{50}$$

where the tilde denotes the rescaled variables, and the transformation coefficients λ_1, λ_2, and λ_3 are calculated as

$$\lambda_1(k_x) = \Phi^{DNS}(k_x)/\Phi^{RBE}(k_x), \tag{51}$$

$$\lambda_2(k_x) = \sqrt{B^{DNS}(k_x)/B^{RBE}(k_x)}, \tag{52}$$

$$\lambda_3(k_x) = k_x \cdot \left(U_c^{DNS}(k_x) - \lambda_2(k_x)U_c^{RBE}(k_x)\right), \tag{53}$$

respectively. Figure 9a, b show the contours of the rescaled space–time energy spectra at $y^+ = 15$ based on the Hanning and rectangular windows, respectively. The DNS results are superimposed for comparison. Figure 9a shows that the contours of rescaled space–time energy spectra based on the Hanning window is close to the DNS contours, especially in the energy-containing scales. In contrast, the contours of space–time energy spectra obatined from the rescaled RBE using rectangular window (Fig. 9b) deviate significantly from the DNS contours due to the spectral leakage. Specifically, the spectra at high frequencies are evidently over-predicted.

5 Conclusions

In this paper, the resolvent-based estimation is utilized to predict the space–time energy spectra in turbulent channel flows. We take the same reference plane as that in Ref. [27], which is located in the logarithmic region. The predicted space–time energy spectra in the buffer layer are close to the DNS results. This observation shows that RBE method has

the capability to predict space–time energy spectra. Furthermore, we evaluate the performance of the RBE method. The main observations are summarized below:

1. The location of the reference plane influences the results of both RMS velocity and space–time energy spectra obtained from the RBE method. The optimal location is $y_r^+ = 39$ for the Reynolds number $Re_\tau = 187$ under investigation. Setting the reference plane to either $y_r^+ < 39$ or $y_r^+ > 39$ results in a less satisfactory predictive performance of the RBE method.
2. The implementation approach of the pressure boundary condition does not influence the results of RMS velocity and space–time energy spectra obtained from the RBE method.
3. The inclusion of pressure as an input does not change the results of the RBE method.
4. A window function is needed in the RBE method to prevent the energy leakage from low to high frequencies in the space–time energy spectra, although it imposes little effect on the streamwise RMS velocity.

Acknowledgements This work was supported by the National Natural Science Foundation of China (Basic Science Center Program for "Multiscale Problems in Nonlinear Mechanics") (Grant 11988102). The authors would like to thank the support from the Strategic Priority Research Program (Grant XDB22040104). Z. Yang also acknowledges the "Lixing" plan of the Institute of Mechanics, Chinese Academy of Sciences.

References

1. He, G.W., Jin, G.D., Yang, Y.: Space–time correlations and dynamic coupling in turbulent flows. Ann. Rev. Fluid Mech. **49**, 51–70 (2017)
2. Graham, W.R.: A comparison of models for the wavenumber-frequency spectrum of turbulent boundary layer pressures. J. Sound Vib. **206**, 541–565 (1997)
3. Bossuyt, J., Meneveau, C., Meyers, J.: Wind farm power fluctuations and spatial sampling of turbulent boundary layers. J. Fluid Mech. **823**, 329–344 (2017)
4. Hao, X., Shen, L.: Wind-wave coupling tudy using LES of wind and phase-resolved simulation of nonlinear waves. J. Fluid Mech. **874**, 391–425 (2019)
5. Moin, P., Mahesh, K.: Direct numerical simulation: a tool in turbulence research. Ann. Rev. Fluid Mech. **30**, 539–578 (1998)
6. Elsinga, G.E., Scarano, F., Wieneke, B., et al.: Tomographic particle image velocimetry. Exp. Fluids. **41**, 933–947 (2006)
7. Schanz, D., Gesemann, S., Schröder, A.: Shake-The-Box: Lagrangian particle tracking at high particle image densities. Exp. Fluids. **57**, 70 (2016)
8. Marusic, I., McKeon, B.J., Monkewitz, P.A., et al.: Wall-bounded turbulent flows at high Reynolds numbers: recent advances and key issues. Phys. Fluids **22**, 065103 (2010)
9. Smits, A.J., McKeon, B.J., Marusic, I.: High-Reynolds number wall turbulence. Annu. Rev. Fluid Mech. **43**, 353–375 (2011)
10. Hu, R., Yang, X., Zheng, X.: Wall-attached and wall-detached eddies in wall-bounded turbulent flows. J. Fluid Mech. **885**, A30 (2020)
11. de Kat, R., Ganapathisubramani, B.: Frequency-wavenumber mapping in turbulent shear flows. J. Fluid Mech. **783**, 166–190 (2015)
12. Wu, T., Geng, C.H., Yao, Y.C., et al.: Characteristics of space-time energy spectra in turbulent channel flows. Phys. Rev. Fluids **2**, 084609 (2017)
13. Wu, T., He, G.W.: Local modulated wave model for the reconstruction of space-time energy spectra in turbulent flows. J. Fluid Mech. **886**, A11 (2020)
14. Kraichnan, R.H.: Kolmogorov's hypotheses and Eulerian turbulence theory. Phys. Fluids **7**, 1723–1734 (1964)
15. Tennekes, H.: Eulerian and Lagrangian time microscales in isotropic turbulence. J. Fluid Mech. **67**, 561–567 (1975)
16. Wilczek, M., Narita, Y.: Wave-number-frequency spectrum for turbulence from a random sweeping hypothesis with mean flow. Phys. Rev. E **86**, 066308 (2012)
17. Wilczek, M., Stevens, R.J.A.M., Meneveau, C.: Spatio-temporal spectra in the logarithmic layer of wall turbulence: large-eddy simulations and simple models. J. Fluid Mech. **769**, R1 (2015)
18. Mansour, N.N., Kim, J., Moin, P.: Reynolds-stress and dissipation-rate budgets in a turbulent channel flow. J. Fluid Mech. **194**, 15–44 (1988)
19. Marusic, I., Mathis, R., Hutchins, N.: Predictive model for wall-bounded turbulent flow. Science **329**, 193–196 (2010)
20. Mathis, R., Huchins, N., Marusic, I.: A predictive inner-outer model for streamwise turbulence statistics in wall-bounded flows. J. Fluid Mech. **681**, 537–566 (2011)
21. Baars, W.J., Huchins, N., Marusic, I.: Spectral stochastic estimation of high-Reynolds number wall-bounded turbulence for a refined inner–outer interaction model. Phys. Rev. Fluids **1**, 054406 (2016)
22. Han, G.W., Liu, L., Bo, T.L., et al.: A predictive model for the streamwise velocity in the near–neutral atmospheric surface layer. J. Geophys. Res. Atmos. **124**, 238–251 (2019)
23. Yin, G., Huang, W.X., Xu, C.X.: Prediction of near-wall turbulence using minimal flow unit. J. Fluid Mech. **841**, 654–673 (2018)
24. Beneddine, S., Sipp, D., Arnault, A., et al.: Conditions for validity of mean flow stability analysis. J. Fluid Mech. **798**, 485–504 (2016)
25. Gómez, F., Blackburn, H.M., Rudman, M., et al.: A reduced-order model of three-dimensional unsteady flow in a cavity based on the resolvent operator. J. Fluid Mech. **798**, R2 (2016)
26. Zare, A., Jovanović, M.R., Georgiou, T.T.: Colour of turbulence. J. Fluid Mech. **812**, 636–680 (2017)
27. Towne, A., Lozano-Durán, A., Yang, X.: Resolvent-based estimation of space-time flow statistics. J. Fluid Mech. **883**, A17 (2020)
28. McKeon, B.J., Sharma, A.S.: A critical-layer framework for turbulent pipe flow. J. Fluid Mech. **658**, 336–382 (2010)
29. Reynolds, W.C., Hussain, A.K.M.F.: The mechanics of an organized wave in turbulent shear flow. Part 3. Theoretical models and comparisons with experiments. J. Fluid Mech. **54**, 163–188 (1972)
30. del Álamo, J.C., Jiménez, J.: Linear energy amplification in turbulent channels. J. Fluid Mech. **559**, 205–213 (2006)
31. Pujals, G., García-Villalba, M., Cossu, C., et al.: A note on optimal transient growth in turbulent channel flows. Phys. Fluids **21**, 015109 (2009)
32. Morra, P., Semeraro, O., Henningson, D.S., et al.: On the relevance of Reynolds tresses in resolvent analyses of turbulent wall-bounded flows. J. Fluid Mech. **867**, 969–984 (2019)
33. Hwang, Y., Cossu, C.: Amplification of coherent streaks in the turbulent Couette flow: an input-output analysis at low Reynolds number. J. Fluid Mech. **643**, 333–348 (2010)
34. Hwang, Y., Cossu, C.: Linear non-normal energy amplification of harmonic and stochastic forcing in the turbulent channel flow. J. Fluid Mech. **664**, 51–73 (2010)

35. Vadarevu, S.B., Symon, S., Illingworth, S.J., et al.: Coherent structures in the linearized impulse response of turbulent channel flow. J. Fluid Mech. **863**, 1190–1203 (2019)
36. Illingworth, S.J., Monty, J.P., Marusic, I.: Estimating large-scale structures in wall turbulence using linear models. J. Fluid Mech. **842**, 146–162 (2018)
37. Cess, R.D.: A survey of the literature on heat transfer in turbulent tube flow. Resarch Report No.8-0529-R24, Westinghouse (1958)
38. Luhar, M., Sharma, A.S., McKeon, B.J.: On the structure and origin of pressure fluctuations in wall turbulence: predictions based on the resolvent analysis. J. Fluid Mech. **751**, 38–70 (2014)
39. Sharma, A.S., McKeon, B.J.: On coherent structure in wall turbulence. J. Fluid Mech. **728**, 196–238 (2013)
40. Liu, C., Gayme, D.F.: An input-output based analysis of convective velocity in turbulent channel flows. J. Fluid Mech. **888**, A32 (2020)
41. Towne, A., Schmidt, O.T., Colonius, T.: Spectral proper orthogonal decomposition and its relationship to dynamic mode decomposition and resolvent analysis. J. Fluid Mech. **847**, 821–867 (2018)
42. Moarref, R., Jovanović, M.R., Tropp, J.A., et al.: A low-order decomposition of turbulent channel flow via resolvent analysis and convex optimization. Phys. Fluids **26**, 051701 (2014)
43. Trefethen, L.N.: Spectral Methods in MATLAB. SIAM, Philadelphia (2000)
44. Deng, B.Q., Xu, C.X.: Influence of active control on STG-based generation of streamwise vortices in near-wall turbulence. J. Fluid Mech. **710**, 234–259 (2012)
45. Yang, Z.X., Wang, B.C.: Capturing Taylor-Görtler vortices in a streamwise-rotating channel at very high rotation numbers. J. Fluid Mech. **838**, 658–689 (2018)
46. Moser, R.D., Kim, J., Mansour, N.N.: Direct numerical simulation of turbulent channel flow up to $Re_\tau = 590$. Phys. Fluids **11**, 943–945 (1999)
47. Choi, H., Moin, P.: On the space-time characteristics of wall-pressure fluctuations. Phys. Fluids **2**, 1450–1460 (1990)
48. del Álamo, J.C., Jiménez, J.: Estimation of turbulent convection velocities and corrections to Taylor's approximation. J. Fluid Mech. **640**, 5–26 (2009)
49. Taylor, G.I.: The spectrum of turbulence. Proc. R. Soc. Lond. A **164**, 476–490 (1938)
50. Liese, F., Vajda, I.: On divergences and informations in statistics and information theory. IEEE Trans. Inf. Theory **8**, 4394–4412 (2006)